

Extended quantitative characterization of solar cell from calibrated voltage-dependent electroluminescence imaging

Cite as: J. Appl. Phys. 129, 043106 (2021); doi: 10.1063/5.0021095

Submitted: 7 July 2020 · Accepted: 3 December 2020 ·

Published Online: 26 January 2021



View Online



Export Citation



CrossMark

Daniel Ory,^{1,2,a)} Nicolas Paul,³ and Laurent Lombez^{2,4}

AFFILIATIONS

¹EDF, 18 Boulevard Thomas Gobert, 91120 Palaiseau, France

²UMR IPVF 9006 18 Boulevard Thomas Gobert, 91120 Palaiseau, France

³EDF, 6 Quai Watier, 78400 Chatou, France

⁴Université de Toulouse, INSA-CNRS-UPS, LPCNO, 135 Avenue Rangueil, 31077 Toulouse, France

^{a)}Author to whom correspondence should be addressed: daniel.ory@edf.fr

ABSTRACT

In this paper, we derived a new method to map various optoelectronic parameters of solar cells from voltage-dependent electroluminescence imaging. To get quantitative data, we show how the voltage dependence of electroluminescence mimics a local diode current–voltage behavior, and we propose a way to measure the absolute electroluminescence flux. We therefore introduce a calibration factor generally left unknown in the literature. Example is shown on the Al-BSF silicon solar cell for which we map several parameters: diffusion lengths, dark saturation current, local voltages, and lumped series resistances with good accuracy. Comparison with other electroluminescence imaging methods is also shown. Preliminary knowledge about the sample are the spectral reflection coefficient, average dopant concentration, and back surface recombination. This method can also be derived for other kinds of solar cells by using an appropriate carrier collection model depending on their structure.

Published under license by AIP Publishing. <https://doi.org/10.1063/5.0021095>

I. INTRODUCTION

Electroluminescence has been known as a powerful experimental tool for the local analysis of solar cells for decades.¹ This technique is easy to implement and has been developed to access different optoelectronic properties.^{2–7} Various fields of application are covered, and this technique is used in research laboratory, industrial production, and outdoor measurement.^{8–12} The spatial information allows one to analyze the influence of inhomogeneities and improve fabrication processes.

As one of the first outcomes of electroluminescence imaging, the diffusion length of minority carriers was measured first by Fuyuki *et al.*² in 2005. The method is based on a single EL image and relates the EL intensity to the diffusion length provided that the diffusion length is much smaller than the thickness of the device. To improve this method, authors like Würfel *et al.*,¹³ followed by Kirchartz *et al.*,¹⁴ proposed to use the ratio of two EL images taken with two different pass-filters. The major advantage is

to cancel the unknown local voltage as well as the spatial and absolute calibration otherwise needed.

One of the most studied parameters by EL imaging is the series resistance. One generally probes a lumped resistance that includes the sheet resistance and the contact resistance and not only the resistance of the local diode. A wide range of techniques already exists. In a book chapter,¹⁵ Bothe and Hinken provide an extended review of the state of the art about this topic, where works from Trupke *et al.*,¹⁶ Rampseck *et al.*,¹⁷ Hinken *et al.*,⁴ Kampwerth *et al.*,¹⁸ Haunschild *et al.*,¹⁹ Breitenstein *et al.*,²⁰ and finally Glatthaar *et al.*⁷ are analyzed and compared. It is not the purpose of this work to redo or comment in detail this review. To our understanding, only the method of Hinken *et al.*⁴ is based on electroluminescence imaging only. The other techniques described require additional experiments like photoluminescence, dark lock-in thermography (DLIT), or light beam induced current (LBIC) to provide additional information, which might be more complicated from the experimental or the industrial point of view.

Other EL mapping techniques are also used, but less studied. Mapping of dark saturation is sometimes linked to the mapping of the series resistance like in the work of Breitenstein *et al.*,²⁰ Glatthaar *et al.*,⁷ and Rajput *et al.*²¹ although the latter cannot provide maps of cells' characteristics but single data for each module's cell. It might also require the use of DLIT like in the work of Ramspeck *et al.*¹⁷ The mapping of the local diode voltage (or implied V_{oc} or quasi-Fermi level splitting) is often obtained by photoluminescence imaging and rarely from electroluminescence.

In addition, the works reported above often suffer from assumptions on parameters or linearization in order to get spatial or absolute calibration. Actually, local absolute calibration of the luminescence is barely achieved in the literature,²² especially regarding intensity electroluminescence imaging. Some existing methods^{28,29} use several images of photo- or electro-luminescence taken in known conditions of illumination and/or voltage to simplify the underlying model, for example, to assume the absence of lateral transport. In some cases, noise in the measurement has a strong negative impact as images are added or subtracted, which can be improved at the expense of spatial resolution. Another method for absolute electroluminescence consists in calibrating the experiment with a known sample, like a homogeneous c-Si solar cell, as in the work of Mochizuki *et al.*³⁰ or Hong *et al.*³¹ To our knowledge, calibration from photometric or radiometric description of the experiment has not previously been reported. A method will be shown below that will give a direct way toward quantitative EL images.

The work presented here aims at exploiting the voltage dependence of the electroluminescence images of a solar cell, each dependence being locally analyzed (i.e., at each pixel location). Appropriate equations describing the optical system sample and setup are established that give access to the local calibration coefficient. By fitting the $EL(V)$ curve with the model built, we then show how several recombination and transport properties like diffusion length, series resistance, local voltage, and radiative and dark saturation current can be accurately extracted as 2D maps with one experiment and high spatial resolution.

II. EXPERIMENTAL SETUP AND SAMPLE

The experiment consists of acquiring a set of electroluminescence images with a small increase in the applied voltage (10 mV) from 0 to 700 mV. We present in the section the sample characteristics and the experimental setup. The modeling of the experimental data will be addressed in Sec. III.

The sample was a classical Al-BSF silicon solar cell with a thickness of 187 μm and a surface of 156.75 \times 156.75 mm². It is composed by a p-doped base wafer with resistivity between 0.87 $\Omega\text{ cm}$ and 0.99 $\Omega\text{ cm}$ and an average value of 0.91 $\Omega\text{ cm}$. This corresponds to a dopant concentration of $1.5 \times 10^{16} \text{ cm}^{-3}$ to $1.7 \times 10^{16} \text{ cm}^{-3}$. The silicon wafer for this cell was grown using cast-mono technology along the [100] direction of the silicon crystal. The combined dark recombination current of the base and rear surfaces was estimated to be 166 fA/cm² according to the method of Wong *et al.*³² adapted to Al-BSF architecture on a Cz wafer. Using Eqs. (6) and (22), and having measured the lifetime of the Cz wafer at about 500 μs , the back surface recombination velocity was estimated to be 100 cm/s. This corresponds to a dark recombination $J_{0,\text{rear}} \sim 100 \text{ fA/cm}^2$ for excess carrier density between 10^{14} cm^{-3} and 10^{15} cm^{-3} by using equations of Klow *et al.*³³ The electrical characteristics of this cell are $V_{oc} = 630 \text{ mV}$, $I_{sc} = 9.17 \text{ A}$, and $\eta = 18.67\%$.

The images were acquired with a camera coupled to an infrared corrected objective of 35 mm focal length on which a 1050 nm short pass filter was fixed. The aperture of the objective was set at f/4 to minimize optical aberrations like vignetting. The acquisition time was set to 3 s to optimize the signal-to-noise ratio and minimize both metastable effects due to continuous current into the cell at the highest voltages and cell heating. The camera was a silicon sCMOS sensor-based camera ORCA Flash v2+ from Hamamatsu. An example of the recorded image is displayed in Fig. 1(a) at 0.68 V.

For current–voltage and bias-dependent electroluminescence measurement, the sample was connected with a dedicated chuck to

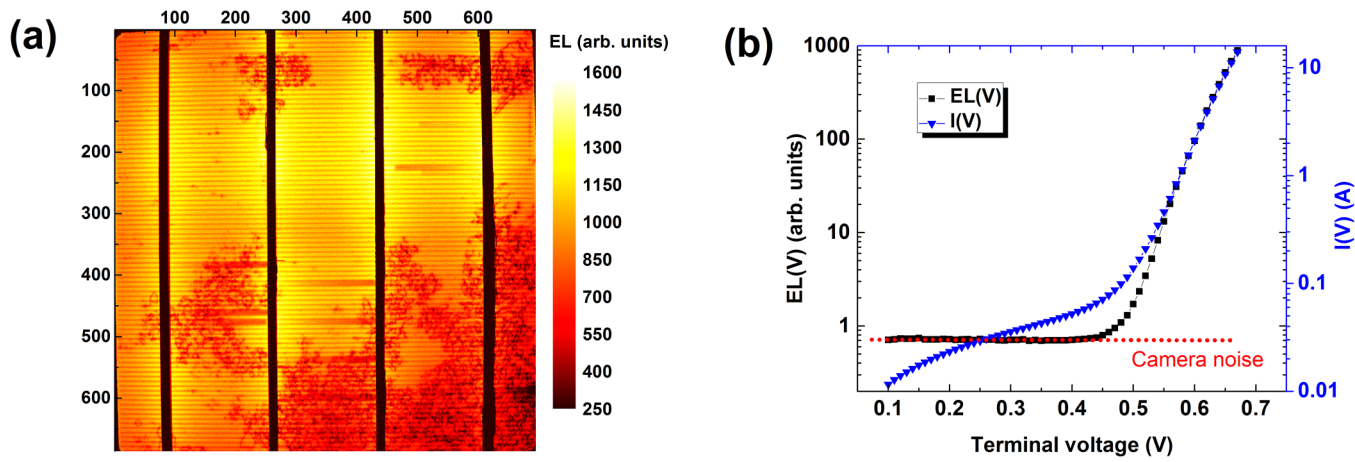


FIG. 1. EL image of the cell at 0.68 V. Coordinates in pixels, 1 pixel = 225 μm ; (b) $EL(V)$ averaged over the cell and $I(V)$ curve of the same.

a sourcemeter Keithley 2651A using a four-probe configuration. The $EL(V)$ pictures and the cell $I(V)$ curve were recorded together. A dark image taken at 0 V bias was recorded and subtracted to all $EL(V)$ pictures. The spatially averaged $EL(V)$ and $I(V)$ curves are shown in Fig. 1(b).

To make the computation faster, the images were resized using a bi-cubic interpolation by a coefficient of 0.4, leading to a spatial resolution of one pixel for $225\ \mu m$ on the cell. The full spatial resolution allowed by the 4Mpix camera is of $90\ \mu m$ per pixel.

III. MODEL AND METHOD

In this section, we will derive the model that will allow to give access to calibrated characteristics of the silicon solar cell. We will separate the modeling of the experiment in different parts. First of all, we will describe the luminescence emission of the solar cell as a function of the voltage and the corresponding intensity of the signal provided by the camera. Next, we will model the light flux from the cell to the sensor, and third, we will model how the camera converts photons to digital units. Eventually, we will link the three models to get a final expression and detail how to obtain quantitative maps of parameters such as diffusion length, saturation current, and series resistance.

A. Electroluminescence emission

Reciprocity relations exist between solar cells and LED.^{34,35} The electroluminescence emission of a solar cell is described by Eqs. (1) and (2). It is driven by the external quantum efficiency EQE , the thermal voltage $vth = kT/q$, the blackbody emission φ_{bb} at temperature T , and E the energy of the photons emitted at the location r of the solar cell,

$$EL(E, V, r) = EQE(E, V, r) \varphi_{bb}(E, T) e^{\left(\frac{V(r)}{vth}\right)}. \quad (1)$$

The blackbody emission being with h the Planck's constant and c the light velocity:

$$\varphi_{bb}(E, T) = \frac{2}{h^3 c^2} \frac{E^2}{e^{\frac{E}{kT}} - 1} \sim \frac{2}{h^3 c^2} E^2 e^{-\frac{E}{kT}}. \quad (2)$$

It must be emphasized that this emission is a spectral radiance, whose unit is $J^{-1} Sr^{-1} s^{-1} m^{-2}$, which we will consider Lambertian.

B. Modeling the experiment

In Fig. 1(b), we can notice that $EL(V)$ graphs match the $I(V)$ curves at voltage above 0.5 V although it is affected by series resistance. It is thus possible to use $EL(V)$ dependence to probe series resistance, and we define an equivalent series resistance R_s^* that applies on the EL signal. It is a fitting parameter playing a similar role on the local EL intensity than the series resistance on the local current density. The extension of Eq. (1) allows us to consider that the local and internal voltages applied for EL emission is the terminal voltage V_T reduced by the effect of R_s^* . We thus write the

voltage-dependent electroluminescence as follows:

$$EL(V_T, E, r) = EQE(E, r) \varphi_{bb}(E, T) e^{\left(\frac{V_T - R_s^*(r) EL(V_T, E, r)}{vth}\right)}. \quad (3)$$

As we are going to study the silicon solar cell, we consider that the quantum efficiency of the solar cell is voltage independent due to the narrow width of the space charge region compared to the overall thickness. This assumption is often made like in the work of Wong and Green³⁶ on generalized reciprocity relation.

C. Current collection

The external quantum efficiency EQE is linked to the internal quantum efficiency IQE by considering the reflectivity $R(E)$ losses,

$$EQE(E) = IQE(E)^*(1 - R(E)). \quad (4)$$

According to Basore in Ref. 37, for absorbed photons with energy above the bandgap and considering the base and rear surfaces only, we have

$$IQE^{-1} = 1 + \frac{\cos(\beta)}{\alpha L_{eff}}. \quad (5)$$

With $\beta \sim 41.3^\circ$, the average path angle of the photons with respect to the cell's normal vector, the absorption coefficient of silicon α ,³⁸ and the effective diffusion length L_{eff} are given by

$$L_{eff} = L \frac{1 + \left(\frac{SL}{D}\right)^* \tanh\left(\frac{W}{L}\right)}{\frac{SL}{D} + \tanh\left(\frac{W}{L}\right)}. \quad (6)$$

The parameters of Eq. (6) are the diffusion length L , the thickness of the quasi-neutral region W , the diffusion coefficient D , and the recombination velocity S of the back surface of the solar cell.

D. Illuminance to the sensor

This part aims at defining a calibration factor in order to measure the absolute intensity of the EL signal. The radiative flux exchanged between two objects, like a cell and a camera sensor, involves the quantification of the medium of propagation as well as the geometry and the relative position of the emission and reception surfaces. The latter are described by the geometrical etendue, a well-known concept inherited from radiometry (or photometry) equations.³⁹

The flux F impinging on the sensor at a certain pixel and the luminance (or radiance) L of the source at the corresponding place r are linked by the following equation, with the assumption of conservation of the etendue,³⁹

$$F(E) = \frac{\pi T_R T_{opt} L_{source}(E, r)}{4 N^2 (1 + |g_y|)^2}. \quad (7)$$

T_R is the transmittance of the ambient atmosphere (~ 1.00) and T_{opt} is the transmittance of the optical system (~ 0.95), and N is

the f-number of the objective. The parameter g_y is the transverse magnification that is found to be 0.06 for our setup configuration.

In addition, as the solar cell is not very small compared to the working distance, a correction factor must be applied. The luminescence of the cell has to be corrected by $\cos^4(\theta)$, with θ the angle between the optical axis and the direction from the center of the objective (lens) to the solar cell pixel.³⁹ For the outermost pixels of a 6" silicon solar cell viewed with a 35 mm lens at 450 mm distance, the correction is about 10%.

Therefore, we have

$$F(E) = \frac{\pi T_R T_{opt} L_{source}(E, r)}{4 N^2 (1 + |g_y|)^2} \cos^4(\theta). \quad (8)$$

The above expressions are valid at any energy of the photon flux. We will consider T and T_{opt} as constants within the recorded luminescence wavelength range. Finally, the number of photons φ_p impinging on the sensor and recorded on a single pixel is obtained by multiplying the flux F by the pixel surface S_{pixel} and the acquisition time t_{acq} ,

$$\varphi_p(E) = F(E) S_{pixel} t_{acq}. \quad (9)$$

Considering the quantum efficiency of the camera $QEcam$ given by the datasheet of the camera supplier, the number of electrons generated into each sensor pixel is as follows:

$$\varphi_e(E) = \varphi_p(E) \cdot QEcam(E), \quad (10)$$

which gives with Eqs. (8) and (11)–(12),

$$\begin{aligned} \varphi_e(E) = & \frac{\pi T_R T_{opt} \cos^4(\theta) S_{pixel} t_{acq}}{4 N^2 (1 + |g_y|)^2} QEcam(E) \\ & \cdot L_{source}(E, r). \end{aligned} \quad (11)$$

The conversion factor of the camera, named G , is the ratio between the number of electrons generated by the absorbed photons and the number of counts as recorded by the camera. It is expressed in e^-/ADU (analog to digital unit), as depicted in Eq. (12). This parameter G is provided by the camera manufacturer or can be calculated from dark and illuminated flat field images. The gain G can be evaluated pixel by pixel⁴⁰ that needs a very accurate measurement and a stable light source. We have here considered a constant value for all the pixels. The spatial distribution of the error is random and does not jeopardize the spatial analysis,

$$G = \frac{\text{Number of } e^-}{\text{Digital counts}}. \quad (12)$$

Therefore, taking into account the *offset* computed by the manufacturer of the camera that is added to the dark and read noise signals, the signal in electrons φ_e is recorded as φ_{ADU} ,

$$\varphi_{ADU} = \frac{\varphi_e}{G} + \text{offset}. \quad (13)$$

Finally, the signal given by the camera for each pixel is

$$\varphi_{ADU}(E) = K_{cal} QEcam(E) \cdot L_{source}(E, r) + \text{offset}, \quad (14)$$

where we define the 2D calibration matrix K_{cal} as

$$K_{cal} = \frac{1}{G} \frac{\pi T_R T_{opt} \cos^4(\theta) S_{pixel} t_{acq}}{4 N^2 (1 + |g_y|)^2}. \quad (15)$$

We would like to point out that all parameters linked to the setup configuration are easy to determine with a good accuracy. It is, therefore, a straightforward way to obtain an absolute measurement of the electroluminescence photons flux. We believe that this result might be of interest for many applications based on luminescence mapping recording.

E. Complete model

As depicted in Eq. (1), $L_{source}(E, r) = EL(E, r, V_T)$. We finally have by integrating over the energy E ,

$$\begin{aligned} ELcam(r, V_T) = & \text{offset} + K_{cal} \cdot e^{\left(\frac{V_T - R_s^* ELcam_0(r, V_T)}{vth}\right)} \cdot \int EQE \\ & \cdot \varphi_{BB} \cdot QEcam \cdot dE. \end{aligned} \quad (16)$$

It is important to notice that the *offset* is a parameter added to the signal after its recording, even if it includes dark or read noise components. A trivial background subtraction can easily get rid of this parameter. Therefore, the voltage-dependent signal is written as

$$ELcam_0(r, V_T) = K_{cal} e^{\left(\frac{V_T - R_s^* ELcam_0(r, V_T)}{vth}\right)} \int EQE \varphi_{BB} QEcam dE. \quad (17)$$

We finally write the model that is applicable for fitting as

$$ELcam(r, V_T) = \text{offset} + J_{0,cam}^* e^{\left(\frac{V_T - R_s^* ELcam_0(r, V_T)}{vth}\right)}. \quad (18)$$

We have introduced the parameters J_0^* and $J_{0,cam}^*$ as

$$J_{0,cam}^* = K_{cal} \quad J_0^* = K_{cal} \int EQE \varphi_{BB} QEcam dE. \quad (19)$$

We use the notation J_0^* because if the camera quantum efficiency $QEcam$ was spectrally constant in the $EL(V)$ emission energy range, the parameter J_0^* would actually equal to the radiative saturation current^{41,42} $\frac{J_{0,rad}}{q}$ as Eq. (19) would become

$$J_{0,cam}^* = QEcam K_{cal} \int EQE \varphi_{BB} dE = QEcam K_{cal} J_{0,rad}/q. \quad (20)$$

We here show typical result of the fitting done on our sample and discuss its accuracy. The mapping of the fitting results $J_{0,cam}^*$ and R_s^* are depicted in Figs. 2(a) and 2(b) as well as the map of the normalized residuals in Fig. 2(c) and two examples of $EL(V)$ data and

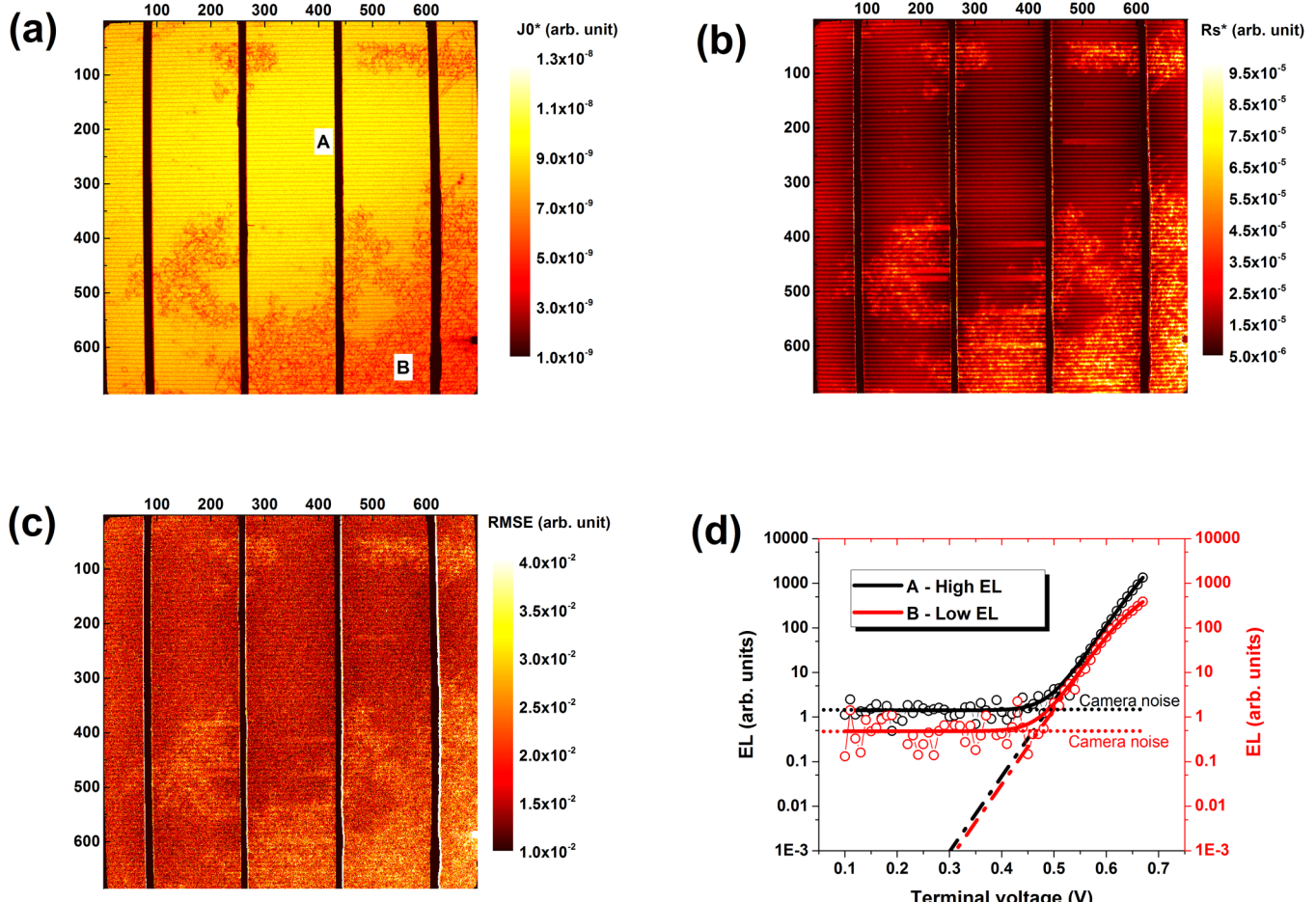


FIG. 2. Results of the fitting for our sample. Coordinates in pixels, 1 pixel = 225 μm . (a) Map of parameter $J_{0,\text{cam}}^*$; (b) map of parameter R_s^* ; (c) map of RMSE; (d) examples of $EL(V)$ curves and fitted curves in one area with low recombination and low series resistance (A—black) and with high recombination and high series resistance (B—red).

the corresponding fitting curves in Fig. 2(d). The average root mean square error (RMSE) is about 0.0189 that shows a very good fitting quality. The experimental curves as in Fig. 2(d) have been chosen in two different areas: one close to a busbar with low series resistance and far from dislocation cluster (A) and the other in a dislocation cluster (B). In Fig. 2(d), the plain curves are the fitted curves including the remaining offset due to noises fluctuation and the dashed curves are the one with this offset subtracted. We clearly see the effect of the series resistance at high voltage which tends to bend the $EL(V)$ curve recorded at the B location. We also notice the difference in pseudo-saturation current $J_{0,\text{cam}}^*$ between both recombination areas by considering the fitted curves without the offset (dashed-dotted curves).

We now discuss the influence of the uncertainty of the parameters of K_{cal} . The relative uncertainties of the parameters are proportional to their power exponent in Eq. (15). Therefore, the most sensitive parameter is the f-number N as shown in Table I. The error on g_y has a minor influence due to its relatively low value

compared to unity, see Eq. (7). Actually, the relative uncertainties on the pixel size, acquisition time, and f-number are negligible thanks to the quality of the camera and the objective. The uncertainty on the measured transmittance T_R and T_{opt} is less than 1%. The overall relative uncertainty on K_{cal} is, therefore, probably comprised between $\pm 1\%$ and $\pm 5\%$.

Another potential origin of error is the variation of lifetime when the excess carrier density varies, which in our experiment may happen when the voltage increases. This will influence the collection length as derived in Sec. III C. The maximum excess minority carrier density in the quasi-neutral region, at the edge of the PN

TABLE I. Influence of the experimental parameters on the calibration factor K_{cal} .

$\pm 5\%$ error on	g_y	$T_R \cdot T_{opt}$	N	G	S_{pixel}	t_{acq}
Influence on K_{cal}	$\pm 0.5\%$	$\pm 5\%$	$\pm 10\%$	$\pm 5\%$	$\pm 5\%$	$\pm 5\%$

junction, writes¹³ $n_e(0) = \frac{n_i^2}{N_A} e^{\frac{V(t)}{V_{sat}}}$. Having $N_A = 1.5 \times 10^{16} \text{ cm}^{-3}$ and $n_i = 7 \times 10^9 \text{ cm}^{-3}$, one obtains $n_e(0)$ on the order of $2 \times 10^{15} \text{ cm}^{-3}$ for local voltage less than 680 mV. This carrier density involves an estimated increase in the diffusion length of a few percent (typically 3%–5%) for local voltages less than 680 mV. Due to local voltage drop caused by the series resistance, the terminal voltage can be slightly higher, and our experiment for which terminal voltage is limited to 700 mV remains in the low error range.

In this section, we have derived how to convert the electroluminescence signal recorded by the camera into an absolute photon flux emitted by the cell with relatively simple inputs describing the setup and the sample. We also discussed the accuracy of this calibration. Hence, we are now able to analyze quantitative mapping of various optoelectronic parameters as it is shown in Secs. IV and V.

IV. RESULTS AND DISCUSSION

A. Extracting diffusion length and dark saturation current maps

According to Eq. (19), we first extract the parameter $J_0^* = \frac{J_{0,cal}}{K_{gal}}$. Then, knowing the back-surface recombination velocity and the spectral reflection coefficient of the sample, we calculate a calibration curve $J_0^*(L_{eff})$. It is obtained by combining Eqs. (5) and (19) and by integrating over the energy. The equation $J_0^*(L_{eff})$ reads as follows:

$$J_0^*(L_{eff}) = \int \frac{(1-R)}{1 + \frac{\cos(\beta)}{\alpha L_{eff}}} \varphi_{BB} Q E_{cam} dE. \quad (21)$$

Therefore, one can attribute a single (effective) diffusion length to each value of J_0^* thanks to Eq. (21) [and Eq. (6) describing L_{eff}] as it is displayed in Fig. 3. If the back SRV is not known, the

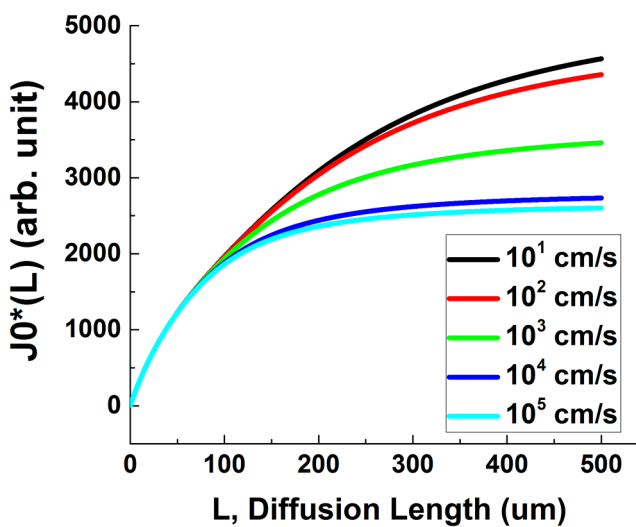


FIG. 3. Calibration curves for the conversion between the parameter J_0^* and the diffusion length for various back surface recombination velocities.

calibration curve can relate J_0^* to the effective diffusion length L_{eff} using Eq. (21) only. By assuming a constant spatial diffusion coefficient and knowing that $L = \sqrt{D \tau}$, calculating the corresponding lifetime map is straightforward. As in the work of Würfel *et al.*,¹³ the uncertainty on the estimation of diffusion length larger than 100 μm is higher if the back surface recombination velocity exhibits strong variation or high uncertainty between 100 cm/s until 10 000 cm/s. High recombination velocities make also the range of discernable diffusion lengths narrower as there is a quasi-plateau of J_0^* for diffusion lengths of 300 μm or higher.

An important remark is that for the multicrystalline silicon solar cell, the spectral reflection coefficient varies depending on the grain orientation. This variation must be taken into account in the calculation of Eq. (21).

We will compare the diffusion length map obtained with our model [see Fig. 4(a) for illustration] with one obtained with another method from Würfel *et al.*¹³ [see Fig. 4(b) for comparison]. The latter method is based on the ratio of two electroluminescence images taken with two different short pass filters. We used two EL images acquired with 900 nm and 1050 nm short pass filters (not corrected for \cos^4 optical artifact) for comparison with our result.

The histograms are displayed in Fig. 4(c) for both methods. From our method, the most frequent value (mode) is about 155 μm and the average about 129 μm. From the EL ratio method,¹³ these values are found to be 156 μm and 160 μm, respectively. Both methods are in good agreement. The spread is, however, slightly different; our method showing an asymmetry toward the low values of diffusion lengths, whereas the ratio method has a quasi-symmetric histogram. The spatial repartition is also slightly different, the EL ratio method exhibiting a vignetting-like inhomogeneity.

Interestingly, the $J_0^*(L)$ curve of the $EL(V)$ method exhibits a high dynamic range as they extend over three orders of magnitude for diffusion lengths between 0.5 μm and 1000 μm, see Fig. 4(d). This allows to easily measure a large range of diffusion lengths from the J_0^* mapping having fitted the $EL(V)$ data. Compared to the corresponding calibration curve—as it is called in the EL ratio method publication¹³—this is particularly true for the extreme values (i.e., low and high diffusion length) where the slope of the $J_0^*(L)$ curves is more pronounced and thus more accurate.

In order to double check the validity of the results, we performed simulation with PC1D. The series resistance, shunt resistance, and photocurrent were set to match the one of the dark and light current–voltages we fitted with a two-diode model^{43,44} and also $S_{front} = S_{back} = 200 \text{ cm/s}$. The results are an efficiency of 18.25% for $L = 129 \mu\text{m}$ [$EL(V)$ method] and 18.6% for $L = 162 \mu\text{m}$ (EL ratio method) for the real efficiency of our cell measured at 18.6%. This shows that we obtained the good consistency of the mapping with our $EL(V)$ method.

To go further into the analysis, we investigated the spatial information given by our diffusion length mapping. The histogram of the data is depicted in Fig. 5(b) and can be fitted with the appropriate numbers of Gaussian distributions. Three distributions can be identified with central values of 107.3 μm, 142.6 μm, and 167.2 μm.

By mapping diffusion length bands around these central values and using appropriate color thresholds, one can identify

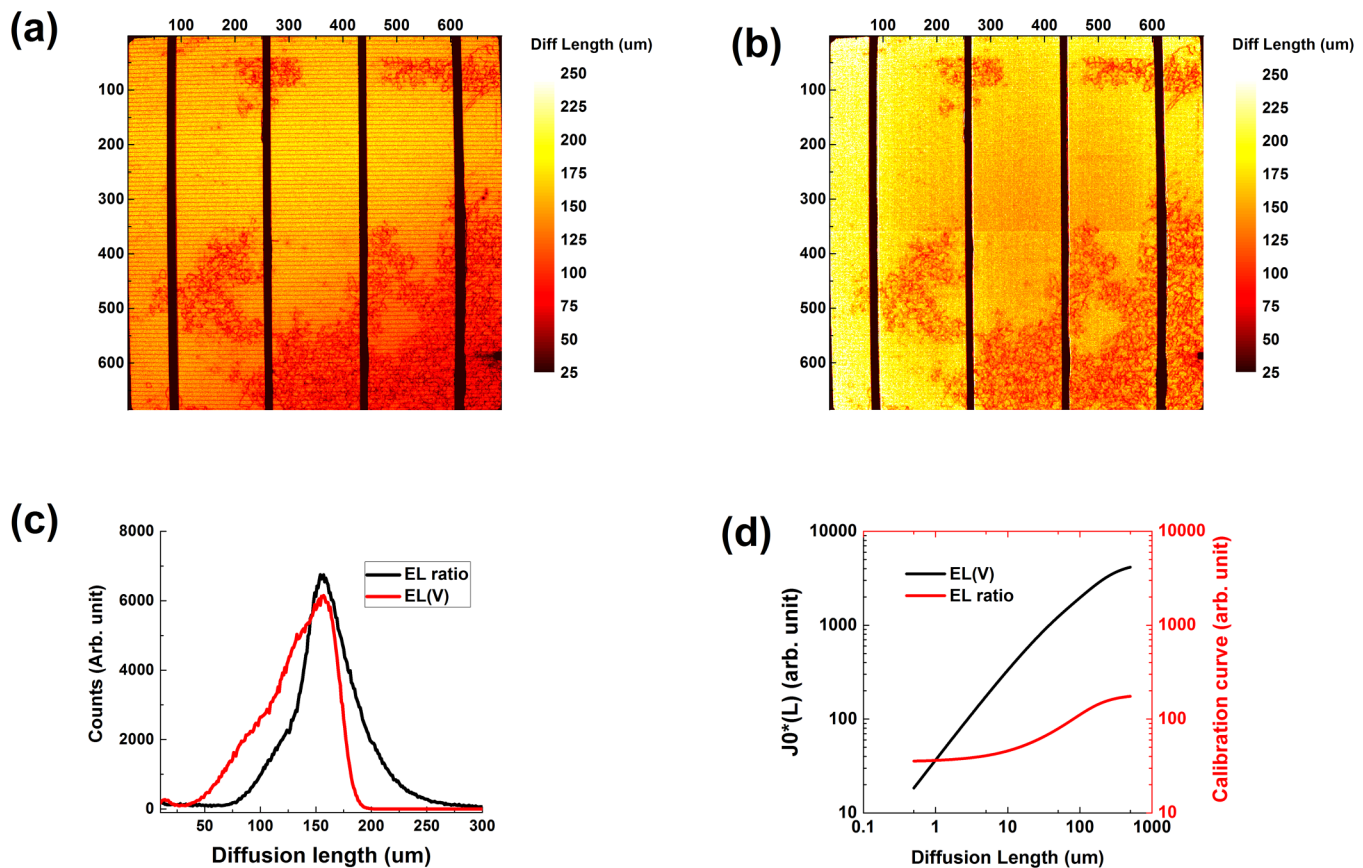


FIG. 4. Diffusion length maps from electroluminescence imaging, coordinates in pixels, 1 pixel = 225 μm . (a) $EL(V)$ method, average = 129 μm , mode = 156 μm ; (b) EL ratio method, average = 160 μm , mode = 156 μm . (c) Corresponding histograms. (d) Calibration curves of $EL(V)$ technique and EL images ratio technique.

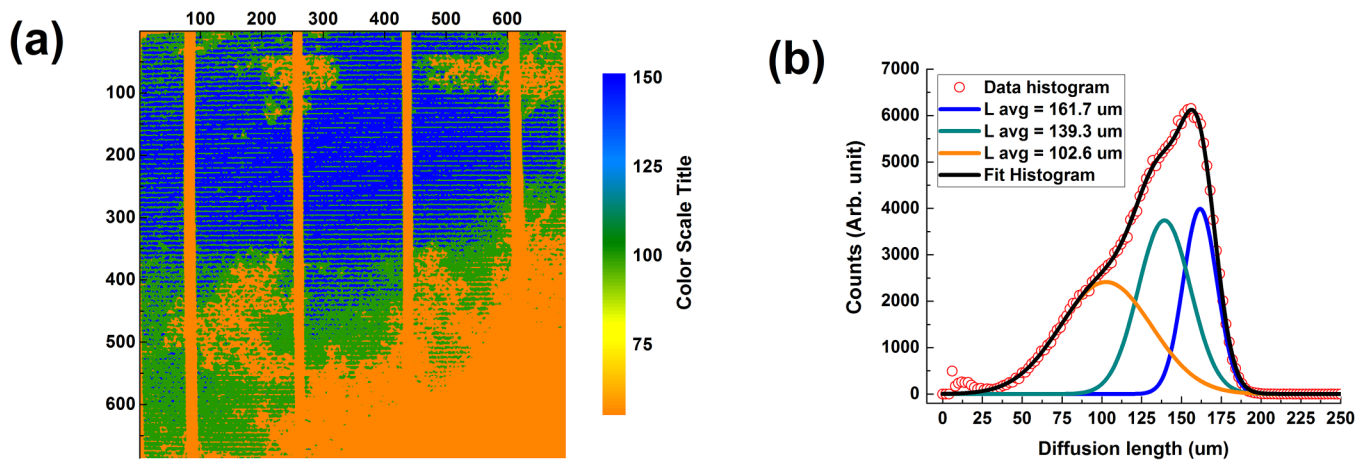


FIG. 5. Threshold image of the diffusion length map. Coordinates in pixels, 1 pixel = 225 μm . The color bar is made according to the repartition histograms in (b) and highlights the three gaussian contributions.

three different spatial areas where the recombination properties are driven by specific root causes [see Fig. 5(a)]. The orange area matches with the dislocation clusters' presence. This might also be decorated by impurities, the most probable being the iron. The blue area with the highest diffusion lengths corresponds to the least contaminated area of the cell, without any detectable dislocation network and with minimum impurity concentration. The purple area is a transition area between the low and high diffusion length areas. It is with high probability the indication of the presence of impurities like iron. Indeed, the wafer was selected in the high solidification fraction of the brick where iron tends to accumulate. The dislocations are diffusion channels for the impurities like iron during the cooling process and later on during gettering due to phosphorus diffusion. They are attractive for impurities that explain their accumulation in the dislocation vicinity. This accumulation could be a marker of non-detectable dislocations by refining spatial resolution and image processing.

From the split of the histogram into three sub-distribution, we also notice that the three zones are mixed together with similar contribution/strength. These three contributions are already noticeable in the global histogram. We deduce from their overlap in the high diffusion length range that high diffusion length pixels still exist all over the cell, even in the dislocation clusters.

The local dark saturation map in the base can be calculated from the effective diffusion length map as explained before, using L_{eff} instead of L , applying Eqs. (21) and (22),

$$J_{0,\text{base}} = q \frac{n_i^2}{N_A} \frac{D}{L_{\text{eff}}} - J_{0,\text{rear}}. \quad (22)$$

The calculation of the local dark saturation current requires the value of the local dopant concentration. The measurement by eddy current gave an average value of $1.5 \times 10^{16} \text{ cm}^{-3}$ and a spread over the cell of $\pm 6\%$, which is low. However, various works in the literature^{45,46} have reported spatial variations of the dopant concentration up to 40%, especially, in the case of small lateral inhomogeneities like grain boundaries and dislocations. This lateral variation might be involved in several phenomena like LeTID.⁴⁷ A variation of 40% on the dopant density has, therefore, an influence of a similar magnitude on the dark saturation current, as shown by Eq. (22), and on the extracted series resistance map, as will be shown later on in Eq. (31). Depending on the spatial resolution of the experiment, the spatial extent of the dopant concentration variations might be noticeable or not. For example, in our experiment, one pixel corresponds to $225 \mu\text{m}$. Very short-range variations should therefore be averaged spatially and have minor influence on dark saturation current and series resistance calculation. For the rest of the paper, we will consider a spatially homogeneous doping density.

Figure 6 depicts the base + rear surface dark saturation current density map. This map exhibits very good contrast and high dynamic range. We can distinguish very low values from the areas the least affected by dislocations and impurities, with values seven times higher than the ones in the dislocations' cluster areas.

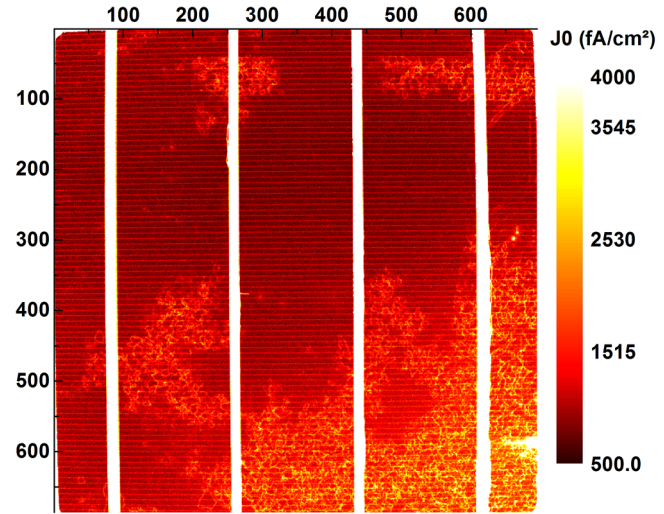


FIG. 6. Map of base + rear surface dark saturation current density in fA/cm^2 . Coordinates in pixels, 1 pixel = $225 \mu\text{m}$.

B. Extracting local voltage and series resistance map

We here probed the local voltage and the series resistance map and discussed the link between the fitted parameter R_s^* and the true quantitative value R_s that applies to the carrier transport within the cell. Following a way close to the one proposed by Hinken *et al.*,⁴ we start with the definition of the local voltage drop. We consider similarly $I(V)$ and $EL(V)$ equations to extract R_s from R_s^* and $J_{0,cam}^*$ in particular. Thus, the local current is affected by the local series resistance R_s and shunt resistance R_{sh} , and we suppose that the local ideality factor is $n = 1$, which is confirmed by fitting the dark $I(V)$ curve. The local voltage drop reads as follows:

$$\Delta V(r) = R_s(r) \left(J(r) + \frac{V(r)}{R_{sh}(r)} \right). \quad (23)$$

The local diode current and the local electroluminescence signal become Eqs. (24) and (25),

$$J(r) = J_0(r) e^{\left(\frac{V_T}{vth}\right)} e^{\left(\frac{-\Delta V(r)}{vth}\right)} = J_0(r) e^{\left(\frac{V(r)}{vth}\right)}. \quad (24)$$

The recombination current $J_0(r)$ is the sum of the recombination current of the base and rear surface $J_{0,\text{base+rear}}$ and the recombination of the emitter $J_{0,e}$ if the latter cannot be neglected,

$$\begin{aligned} ELcam_0(V, r) &= J_{0,cam}^*(r) e^{\left(\frac{V_T}{vth}\right)} e^{\left(\frac{-R_s^*(r) ELcam_0(V_T, r)}{vth}\right)} \\ &= J_{0,cam}^*(r) e^{\left(\frac{V(r)}{vth}\right)}. \end{aligned} \quad (25)$$

We deduce from Eq. (25) that

$$\Delta V(r) = R_s^*(r) ELcam_0(V_T, r). \quad (26)$$

By rearranging and combining Eqs. (23)–(25), we obtain

$$R_s(r) = \frac{R_s^*(r) ELcam_0(r)}{\frac{J_0(r) ELcam_0(r)}{J_{0,cam}^*} + \frac{V(r)}{R_{sh}(r)}}. \quad (27)$$

As we have from Eq. (25), the local voltage

$$V(r) = vth \ln\left(\frac{ELcam_0}{J_{0,cam}}\right). \quad (28)$$

We conclude that the local series resistance reads as follows:

$$R_s(r) = \frac{R_s^*(r) \frac{J_{0,cam}}{J_0(r)}}{1 + \frac{vth}{J_0(r) ELcam_0(r) R_{sh}(r)} \ln\left(\frac{ELcam_0}{J_{0,cam}}\right)}. \quad (29)$$

In the limiting case where the electroluminescence intensity is high enough, the series resistance can be expressed in a much simpler form as depicted in Eq. (30), whatever the shunt resistance value is. As the series resistance is constant, we assume that Eq. (30) is the relevant derivation, whereas Eq. (30) depicts the non-trivial relationship between electroluminescence and series and shunt resistances. The rest of the discussion will focus on R_s^∞ only. The local saturation current $J_0(r)$ comes from Eq. (22) where the effective diffusion length is obtained as described above,

$$R_s^\infty(r) = R_s^*(r) \frac{J_{0,cam}}{J_0(r)}. \quad (30)$$

The local voltage map obtained for our sample is depicted in Fig. 7(a). It exhibits a low spatial amplitude of about 16 mV. This is coherent with the fact that the series resistance is also low and

spatially homogeneous, as we will see later on. The series resistance R_s^∞ map obtained for our sample is depicted in Fig. 7(b).

Before discussing our results, we will compare the outcome of our method with two other calculations proposed in the literature. The first method is the work of Hinken *et al.*⁴ already mentioned, because it is also based on voltage-dependent electroluminescence. The second work is based on the transfer function as initiated first by Donolato⁴⁸ and developed by Wong and Green.³⁶

In the work of Hinken *et al.*,⁴ the local series resistance is calculated by fitting a linear equation $\frac{\partial EL}{\partial V} = a \frac{\partial EL}{\partial V} + b$ obtained by differentiating an arrangement of Eqs. (23)–(25). The map obtained is afterward calibrated by a single coefficient assuming that the local saturation current density is spatially constant, which leads to a non-spatial calibration. This inconveniency is mentioned by the authors themselves who recommend their method for monocrystalline cells. As a result of the absence of spatial calibration, the map depicted in Fig. 8(a) (arbitrary units) looks like the *EL* intensity map and is therefore very different from our result. Due to differentiating, the fitting of this method is very sensitive to noise and the adjusted- R^2 can be very low depending on the spatial resolution. Here, the data pixels were binned by 10 and average adjusted- R^2 is 0.38. If the data pixels were binned to 2.5 as in the maps we exhibit otherwise, the adjusted- R^2 would tend to zero in average. This makes this method difficult for high spatial resolution mapping.

The transfer function as derived by Wong *et al.*³⁶ aims at describing the increase in local current involved and the increase in voltage at the device terminal. This generalizes the reciprocity relation between solar cells and LED as described by Rau.³⁴ Assuming a non-voltage-dependent local quantum efficiency, the transfer function reads as follows:

$$f_T = \frac{\partial \ln(EL)}{\partial \frac{qV_T}{kT}}. \quad (31)$$

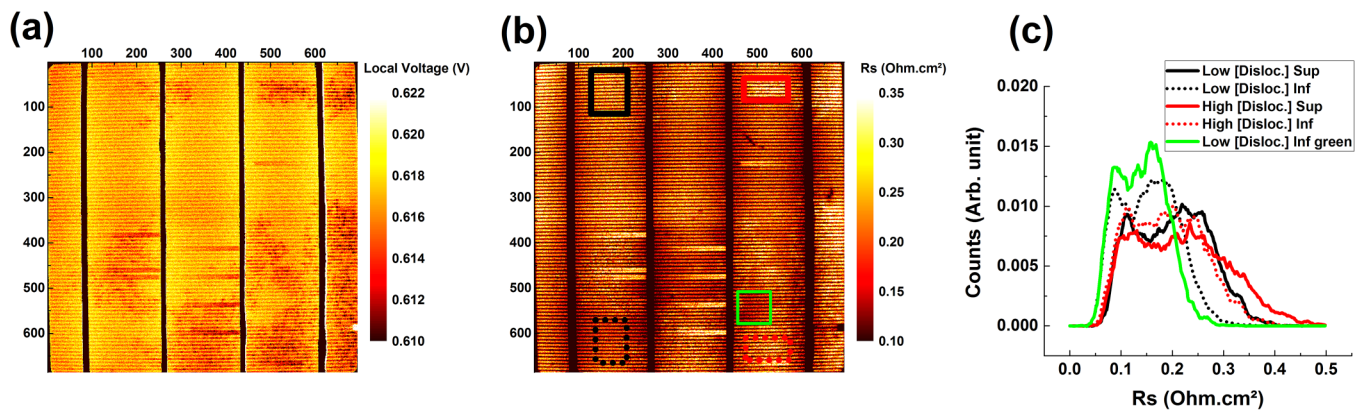


FIG. 7. Coordinates in pixels, 1 pixel = 225 μm . (a) Local voltage at $V = V_{\text{oc}} = 0.63$ V. (b) R_s^∞ map in Ωcm^2 . (c) histograms of R_s^∞ in different zones mixing high/low content of dislocation loops and high/low concentration of impurity (dark/red and solid/dashed contours). In green is reported the histogram of a zone with high content of impurity but low content of dislocations.

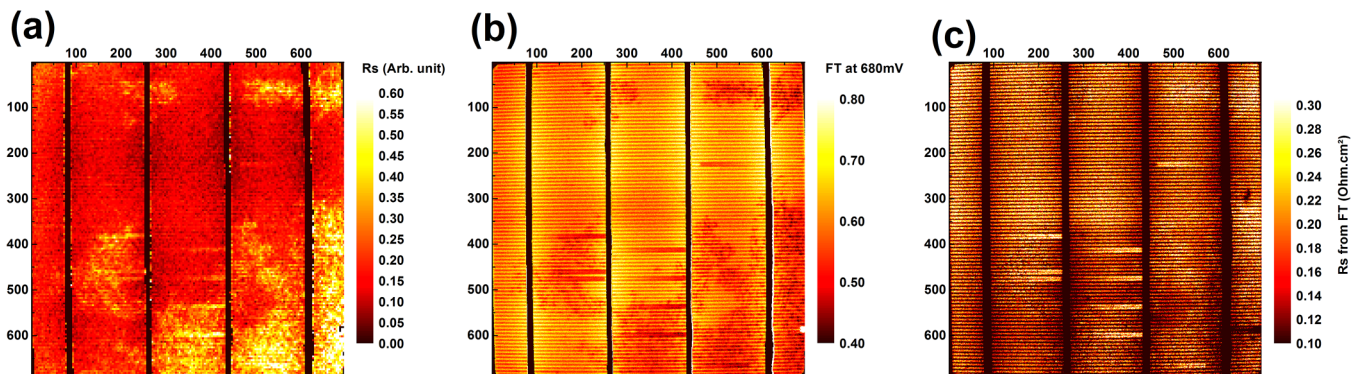


FIG. 8. For comparison: (a) R_s map in arbitrary units (w/o calibration) according to the method proposed by Hinken *et al.*,⁴ pixels binned by factor 10; (b) transfer function as in Wong *et al.*,³⁶ (c) R_s map derived from the transfer function map, as in Wong *et al.*³⁶ All coordinates in pixels, 1 pixel = 225 μm .

This is a voltage-dependent value that tends to 1 when voltage and current are low (high collection efficiency) and decreases with increasing voltage as the collection efficiency becomes reduced. It has, therefore, a link with the series resistance as derived by Wong and Green,³⁶

$$R_s(r) = \left(\frac{1}{f_T(r)} - 1 \right) \Big/ \frac{dJ}{dV}(r), \quad (32)$$

$$\frac{dJ}{dV} = \frac{J_0}{v_{th}} \exp\left(\frac{V(r)}{v_{th}}\right) = \frac{J_0}{J_{0,cam}} \frac{ELcam_0}{v_{th}}. \quad (33)$$

The transfer function f_T is depicted in Fig. 8(b) for 0.68 V and is very similar to the series resistance map derived with the method proposed by Hinken *et al.*⁴ Therefore, considering Eq. (31), the series resistance map could be similar to the transfer function only if the term $\frac{dJ}{dV}(r)$ were spatially constant. This is not the case as it depends on spatially variable parameters as depicted in Eq. (33). The transfer function is then not a direct image of the series resistance and must be properly interpreted. The transfer function is an image of the current flow, but also of the carrier recombination. As a comparison, the complete series resistance map is obtained by combining Eqs. (32) and (33) as depicted in Fig. 8(c) for 0.68 V. It is coherent with our observation regarding spatial repartition and magnitude, see Fig. 7(b) for comparison.

Now if we look at the results we obtained, see Fig. 7(b), the main qualitative remark is that the series resistance is roughly constant all over the cell and that the dislocation clusters have a similar level of series resistance than the rest of the cell. This is coherent with the fact that the average series resistance fitted from $I(V)$ data barely varies while the dislocation content increases within the height of the brick. The areas close to the contact are less resistive, which is logical as the series resistance we measure are lumped values. Classically, corrupt processed fingers appear with series resistance twice higher than the surrounding.

The average value of our series resistance map is about $0.16 \Omega \text{ cm}^2$, while it has been evaluated at $0.25 \Omega \text{ cm}^2$ by fitting the dark $I(V)$ curve that is another confirmation of the relevancy of our

method. The small difference can probably be explained by the uncertainty of the components of the calculation.

We have selected in the series resistance map in Fig. 7(b) areas with low or high content of dislocations (contours in black and red, respectively) and areas with low or high content of impurities (solid or dashed contours, respectively). It can be seen that the dislocation clusters slightly increase the series resistance. In addition, we notice that the areas with low content of impurity (corresponding to areas with low values of J_0 , see Fig. 6) have higher series resistance values whatever the presence of dislocations. This is also noticeable in the area without dislocations and very high content of impurities [green contour in Fig. 7(c)] where the series resistance is significantly lower. It sounds logical that the series resistance is lower where the dopant concentration has been shown to be higher. These correlations, together with the relatively constant R_s map, have to be further investigated, for example, by looking at areas where impurities tend to concentrate due to gettering and/or the presence of dislocations.

V. CONCLUSION

We derived new calculations and a method to map several key parameters of solar cells from voltage-dependent electroluminescence imaging. In particular, we propose a calibration method to record absolute electroluminescence intensity maps. We derived several mappings such as diffusion length map, dark saturation current map, local voltage map, and lumped series resistance map. The method was shown to be complete, accurate, and in good agreement with the use of several previous EL imaging methods. A few assumptions were made, the main one being the homogeneous quantum efficiency and the gain of the camera over the sensor, a constant diffusion coefficient, and a constant ideality factor. Prior compulsory knowledges are the solar cell spectral reflection coefficient, the average dopant concentration, the back surface recombination velocity, and the characteristics of the camera and the optical path. Our method was derived by using the appropriate function for the internal quantum efficiency for the Al-BSF silicon solar cell. However, other kinds of solar cells can be characterized by using the appropriate in-depth collection function.

DATA AVAILABILITY

The data that support the findings of this study are available from the corresponding author upon reasonable request.

REFERENCES

- ¹K. S. Lim, M. Konagai, and K. Takahashi, *Jpn. J. Appl. Phys.* **21**, L473 (1982).
- ²T. Fuyuki, H. Kondo, T. Yamazaki, Y. Takahashi, and Y. Uraoka, *Appl. Phys. Lett.* **86**, 262108 (2005).
- ³T. Fuyuki, H. Kondo, Y. Kaji, A. Ogane, and Y. Takahashi, *J. Appl. Phys.* **101**, 023711 (2007).
- ⁴D. Hinken, K. Ramspeck, K. Bothe, B. Fischer, and R. Brendel, *Appl. Phys. Lett.* **91**, 182104 (2007).
- ⁵T. Kirchartz, U. Rau, M. Kurth, J. Mattheis, and J. H. Werner, *Thin Solid Films* **515**, 6238 (2007).
- ⁶O. Breitenstein, J. Bauer, T. Trupke, and R. A. Bardos, *Prog. Photovolt. Res. Appl.* **16**, 325 (2008).
- ⁷M. Glatthaar, J. Giesecke, M. Kasemann, J. Haunschild, M. The, W. Warta, and S. Rein, *J. Appl. Phys.* **105**, 113110 (2009).
- ⁸T. Potthoff, K. Bothe, U. Eitner, D. Hinken, and M. Köntges, *Prog. Photovolt. Res. Appl.* **18**, 100 (2010).
- ⁹A. Helbig, T. Kirchartz, R. Schaeffler, J. H. Werner, and U. Rau, *Sol. Energy Mater. Sol. Cells* **94**, 979 (2010).
- ¹⁰C. J. Hibberd, F. Plyta, C. Monokroussos, M. Bliss, T. R. Betts, and R. Gottschalg, *Sol. Energy Mater. Sol. Cells* **95**, 123 (2011).
- ¹¹B. Li, A. Stokes, and D. M. J. Doble, *Prog. Photovolt. Res. Appl.* **20**, 936 (2012).
- ¹²R. Ebner, B. Kubicek, G. Újvári, and K. Berger, *Jpn. J. Appl. Phys.* **54**, 08KG02 (2015).
- ¹³P. Würfel, T. Trupke, T. Puzzer, E. Schäffer, W. Warta, and S. W. Glunz, *J. Appl. Phys.* **101**, 123110 (2007).
- ¹⁴T. Kirchartz, A. Helbig, and U. Rau, *Sol. Energy Mater. Sol. Cells* **92**, 1621 (2008).
- ¹⁵K. Bothe and D. Hinken, *Semiconductor and Semimetals* (Elsevier, 2013), pp. 259–339.
- ¹⁶T. Trupke, E. Pink, R. A. Bardos, and M. D. Abbott, *Appl. Phys. Lett.* **90**, 093506 (2007).
- ¹⁷K. Ramspeck, K. Bothe, D. Hinken, B. Fischer, J. Schmidt, and R. Brendel, *Appl. Phys. Lett.* **90**, 153502 (2007).
- ¹⁸H. Kampwerth, T. Trupke, J. W. Weber, and Y. Augarten, *Appl. Phys. Lett.* **93**, 202102 (2008).
- ¹⁹J. Haunschild, M. Glatthaar, M. Kasemann, S. Rein, and E. R. Weber, *Phys. Status Solidi RRL Rapid Res. Lett.* **3**, 227 (2009).
- ²⁰O. Breitenstein, A. Khanna, Y. Augarten, J. Bauer, J.-M. Wagner, and K. Iwig, *Phys. Status Solidi RRL Rapid Res. Lett.* **4**, 7 (2010).
- ²¹A. S. Rajput, *Sol. Energy* **173**, 201 (2018).
- ²²A. Delamarre, L. Lombez, and J.-F. Guillemoles, *J. Photonics Energy* **2**, 027004 (2012).
- ²³P. Würfel, *J. Phys. C Solid State Phys.* **15**, 3967 (1982).
- ²⁴S. Knabe, L. Gütay, and G. H. Bauer, *Thin Solid Films* **517**, 2344 (2009).
- ²⁵B. E. Pieters, T. Kirchartz, T. Merdzhanova, and R. Carius, *Sol. Energy Mater. Sol. Cells* **94**, 1851 (2010).
- ²⁶J. K. Katahara and H. W. Hillhouse, *J. Appl. Phys.* **116**, 173504 (2014).
- ²⁷A. Delamarre, L. Lombez, and J.-F. Guillemoles, *Appl. Phys. Lett.* **100**, 131108 (2012).
- ²⁸M. Glatthaar, J. Haunschild, R. Zeidler, M. Demant, J. Greulich, B. Michl, W. Warta, S. Rein, and R. Preu, *J. Appl. Phys.* **108**, 014501 (2010).
- ²⁹H. Höffler, H. Al-Mohtaseb, J. Haunschild, B. Michl, and M. Kasemann, *J. Appl. Phys.* **115**, 034508 (2014).
- ³⁰T. Mochizuki, C. Kim, M. Yoshita, J. Mitchell, Z. Lin, S. Chen, H. Takato, Y. Kanemitsu, and H. Akiyama, *J. Appl. Phys.* **119**, 034501 (2016).
- ³¹J. Hong, Y. Wang, Y. Chen, X. Hu, G. Weng, S. Chen, H. Akiyama, Y. Zhang, B. Zhang, and J. Chu, *Prog. Photovolt. Res. Appl.* **28**, 295–306 (2019).
- ³²J. Wong, S. Duttagupta, R. Stangl, B. Hoex, and A. G. Aberle, *IEEE J. Photovolt.* **5**, 619 (2015).
- ³³F. Kløw, H. Haug, and S. E. Foss, *Energy Procedia* **43**, 18 (2013).
- ³⁴U. Rau, *Phys. Rev. B* **76**, 085303 (2007).
- ³⁵T. Kirchartz, A. Helbig, W. Reetz, M. Reuter, J. H. Werner, and U. Rau, *Prog. Photovolt. Res. Appl.* **17**, 394 (2009).
- ³⁶J. Wong and M. A. Green, *Phys. Rev. B* **85**, 235205 (2012).
- ³⁷P. A. Basore, *IEEE Trans. Electron Devices* **37**, 337 (1990).
- ³⁸M. A. Green and M. J. Keevers, *Prog. Photovolt. Res. Appl.* **3**, 189 (1995).
- ³⁹J.-L. Meyzonnette and T. Lépine, *Bases de Radiométrie Optique* (Cépadues Editions, 2001).
- ⁴⁰J. R. Janesick, K. P. Klaasen, and T. Elliott, *Opt. Eng.* **26**, 972 (1987).
- ⁴¹D. Abou-Ras, T. Kirchartz, and U. Rau, *Advanced Characterization Techniques for Thin Film Solar Cells* (Wiley-VCH, 2016).
- ⁴²P. Würfel and U. Würfel, *Physics of Solar Cells*, 3rd ed. (Wiley-VCH, 2016).
- ⁴³S. Suckow, T. M. Pletzer, and H. Kurz, *Prog. Photovolt. Res. Appl.* **22**, 494 (2014).
- ⁴⁴O. Breitenstein and S. Riisland, *Sol. Energy Mater. Sol. Cells* **110**, 77 (2013).
- ⁴⁵S. Y. Lim, M. Forster, X. Zhang, J. Holtkamp, M. C. Schubert, A. Cuevas, and D. Macdonald, *IEEE J. Photovolt.* **3**, 7 (2013).
- ⁴⁶T. Mcchedlidze and J. Weber, *Phys. Status Solidi A* **216**, 1900142 (2019).
- ⁴⁷D. Chen, M. V. Contreras, A. Ciesla, P. Hamer, B. Hallam, M. Abbott, and C. Chan, *Prog Photovolt Res Appl.* (published online, 2020).
- ⁴⁸C. Donolato, *Inverse Probl.* **2**, L31 (1986).